REVIEW PAPER

Growth and Plasma Functionalization of Carbon Nanotubes

Shahzad Hussain · Roger Amade · Eric Jover · Enric Bertran

Abstract   This review presents recent results about the growth of vertically aligned carbon nanotubes (VACNTs) by plasma enhanced chemical vapor deposition (PECVD) and water assisted CVD. Modification of VACNTs by surface specific plasma treatments as well as by MnO_2 electrodeposition, allows the optimization of the CNTs physico-chemical properties. Incorporation of oxygen and nitrogen functional groups by oxygen plasma, water plasma and nitrogen plasma are discussed in detail. The surface modification not only decorates the CNTs with desired functional groups, but also increases their surface area and makes them suitable for electrochemical, biological and environmental applications. In order to study the effects of surface functionalization on the CNTs properties, electrochemical and adsorption/desorption measurements were carried out. Both plasma treatments and manganese oxide electrodeposition improve the specific capacitance of the CNTs. Nanocomposites of CNTs/MnO_2 show high specific capacitance values of up to 750 Fg^{-1}. In addition, gas–surface interactions between functionalized and non-functionalized nanotubes, and volatile organic compounds, clearly show enhanced adsorption properties of the surface-modified nanotubes.

Keywords   Plasma treatment · CNTs · Surface functionalization

Introduction

In 1991 Ijima noticed elongated hollow structures in carbon soot, which were MWCNTs, including double-wall nanotubes [1]. The actual experimental discovery

S. Hussain · R. Amade · E. Jover · E. Bertran (✉)
FEMAN Group, IN2UB, Dept. Fisica Aplicada i Optica, Universitat de Barcelona,
Marti I Franques 1, 08028 Barcelona, Catalonia, Spain
e-mail: ebertran@ub.edu

of nanotubes with single walls occurred in 1993 in back to back articles by two separate groups [2, 3]. After 1991, considerable attention of scientists to carbon nanotubes (CNTs) caused remarkable increase of publication around carbon nanotube related subjects of interests.

Carbon nanotubes have gained in interest as nanoscale materials due to their remarkable physical properties such as their very high Young's modulus, their ultimate strength and their high electric and thermal conductivity. Average Young's modulus values of 1.8 and 1.25 TPa were obtained for MWCNTs and SWCNTs, respectively [4, 5]. Quantum mechanics calculations predict that defect-free single-walled carbon nanotubes possess Young's modulus values of 1 TPa, tensile strengths of 100 GPa, and multiwalled carbon nanotubes with a mean fracture strength >100 GPa [6]. For illustration, a tensile strength of 200 GPa for MWCNT corresponds to the ability to endure a weight of 20 tons on a cable with a cross-section of 1 mm^2. Carbon nanotubes thus represent the strongest and stiffest materials in terms of tensile strength and elastic modulus. Experimental thermal conductivity measured on individual MWCNTs reaches 3300 W/(m K), which is about twice as high as diamond [7]. Moreover, CNTs are thermally stable up to 2800 °C in vacuum and up to 700 °C under air [8]. Other important physical properties of CNTs are their electronic properties, which are dependent on the molecular structure (chirality) of CNTs [9]. In 2005 Li *et al.* showed a multichannel quasiballistic conducting behavior occurring in the MWCNTs with large diameter, which can be attributed to the participation of multiple walls in electrical transport and the large diameter of the MWCNTs [10]. The metallic CNTs can carry enormous current densities up to 10^9 A/cm^2 without being destroyed [11]. This density is about 2–3 orders of magnitude higher than the current density of metals such as copper. A high electrical conductivity value of 10^3 S/cm is often measured by both two- and four-probe processes on individual SWCNTs and MWCNTs [12, 13]. Carbon nanotube reactivity is directly related to the pi-orbital mismatch caused by an increased curvature. Therefore, a distinction must be made between the sidewall and the end caps of a nanotube. For the same reason, a smaller nanotube diameter results in increased reactivity.

The unique and extraordinary properties of the CNTs, such as, extremely high electrical and thermal conductivities, very small diameters (less than 100 nm), large aspect ratios (length/diameter ratios, greater than 1000), outstanding mechanical properties, a tip-surface area near the theoretical limit (the smaller area of the tip-surface, the more concentrated electric field, and the largest enhancement factor of the electric field) and an excellent price-performance ratio, make it an ideal candidate for electronic devices, chemical/electrochemical and biosensors, electron field emitters, lithium-ion batteries, white light sources, hydrogen storage cells, cathode ray tubes (CRTs), electrostatic discharge (ESD) and electrical-shielding applications. It is possible to make transistors based on carbon nanotubes that operate at room temperature and can function as a digital switch using a single electron. Worldwide commercial interest in carbon nanotubes (CNTs) is reflected in a production capacity that presently exceeds several thousand tons per year.

Due to these extraordinary properties, CNTs are an attractive material for various applications such as in biology, electrochemistry, etc. However, it remains several

drawbacks to be overcome such as their tendency to become aggregated. Indeed, CNTs form long bundles thermodynamically stabilized by numerous π–π interactions between sidewalls. As well as most of the desired applications require to craft their surface with desired functional groups in order to change their surface properties. Synthesized CNTs present defects and usually, around 1–3 % of carbon atoms of a nanotube are located at a defect site. The end caps of nanotubes can be composed of highly curved fullerene-like hemispheres, which are highly reactive as compared to the sidewalls. The sidewalls themselves contain defect sites such pentagon–heptagon pairs called Stone–Wales defects, sp3-hybridized defects and vacancies in the nanotube lattice [14].

For most applications, like in biology and aqueous electrolytes for supercapacitor applications, it is important to have oxygen functional groups attached to the surface of the nanotubes. Physical or chemical methods can be adopted for the surface treatment of the CNTs. During the functionalization, functional groups or nanoparticles can form a covalent (chemical) or a non-covalent (physical) bond with the CNT surface [15]. In addition post synthesis treatment also enables to remove the amorphous carbon and catalysts particles from the nanotubes.

In this article we review different CNT growth techniques, focusing mainly, on chemical vapor deposition (CVD). Also, we report current functionalization methods used to modify the surface of CNTs and improve their physico-chemical properties. Electrochemical characterization and gas–surface interactions between functionalized and non-functionalized nanotubes, and volatile organic compounds (VOCs), are provided in the last sections.

Synthesis of CNTs

Carbon nanotubes are generally produced by three main techniques, arc discharge, laser ablation and chemical vapor deposition. In arc discharge, a vapor is created by an arc discharge between two carbon electrodes with or without catalyst. Nanotubes self-assemble from the resulting carbon vapor. In the laser ablation technique, a high-power laser beam impinges on a volume of carbon containing feedstock gas (mainly Ar). At the moment, laser ablation produces a small amount of clean nanotubes, whereas arc discharge methods generally produce large quantities of impure material.

Chemical vapor deposition (CVD) is the most prominent technique to synthesize the CNTs. It is also known as thermal CVD or catalytic CVD. In general, chemical vapor deposition (CVD) results in MWCNTs or poor quality SWCNTs. The SWCNTs produced with CVD have a large diameter range, which can be poorly controlled. As compared to arc-discharge and laser-ablation methods, CVD is a simple and economic technique for synthesizing CNTs at low temperature and ambient pressure.

The CVD method uses a carbon source in the gas phase and a heated coil, to transfer the energy to the gaseous carbon molecule. Commonly used carbon sources are methane, carbon monoxide and acetylene. The energy source cracks the molecule into atomic carbon. The carbon then diffuses towards the substrate, which

is heated and coated with a catalyst (usually a first row transition metal such as Ni, Fe or Co) and binds to it [16]. CVD is versatile in the sense that it offers harnessing plenty of hydrocarbons in any state (solid, liquid or gas), enables the use of various substrates, and allows CNT growth in a variety of forms, such as powder, thin or thick films, aligned or entangled, straight or coiled nanotubes, or a desired architecture of nanotubes on predefined sites of a patterned substrate. It also offers better control on the growth parameters [17]. The growth mechanism of CNTs is still somewhat controversial. The suggested mechanisms for the growth of CNTs are vapor–liquid–solid (VLS) theory [18–20] and vapor–solid–solid (VSS) [21]. Few basic steps are generally acknowledged in chemical CNT production regardless of whether the growth takes place in the gas phase or on a supported surface. The catalyst is generally prepared by sputtering a transition metal onto a substrate, followed by etching with chemicals such as ammonia, or thermal annealing, to induce the nucleation of catalyst particles. Thermal annealing results in metal cluster formation on the substrate, from which the nanotubes grow. The temperature for the synthesis of nanotubes using CVD is generally in the 650–900 °C range. When hydrocarbon vapor comes in contact with the "hot" metal nanoparticles decomposes into carbon and hydrogen species; hydrogen flies away and carbon gets dissolved into the metal. After reaching the carbon-solubility limit in the metal at that temperature, as-dissolved carbon precipitates out and crystallizes in the form of a cylindrical network having no dangling bonds and hence energetically stable. Hydrocarbon decomposition (being an exothermic process) releases some heat to the metal's exposed zone, while carbon crystallization (being an endothermic process) absorbs some heat from the metal's precipitation zone. This precise thermal gradient inside the metal particle keeps the process on.

Plasma Enhanced Chemical Vapor Deposition (PECVD)

Growth of MWCNTs by CVD is a very promising technology that allows precise control over the length, diameter and positioning [17]. Particularly, plasma enhanced chemical vapor deposition (PECVD) [22] is an excellent technique to grow vertically aligned carbon nanotubes (VACNTs), which are suited for many applications. It is generally accepted that VLS description presented by Baker et al. [18] for carbon filament growth is also applicable to carbon nanotube growth, at least when metal catalyst particles are employed. In the field of microelectronic application, controllable assembly and directional in situ synthesis of CNTs are very crucial steps to incorporate CNTs directly into the integrated circuit. However, the synthesis of CNTs using CVD method requires undesirably high temperature, which damages the electronic chip. The PECVD process present several advantages such as; low-temperature synthesis of CNTs, vertical alignment due to the electric field, and exposure of the graphitic edge planes due to plasma etching of the walls, which improves electronic transfer in electrochemical applications [23]. Although thermal CVD is more economic and simple, it requires higher temperatures and the obtained CNTs are usually curly and with less defects. Thus, PECVD technique is useful for sensors and/or electrochemical devices where a high specific area and good electron transfer kinetics are needed, as well as low synthesis temperature.

In order to prevent the deposition of amorphous carbon ("a-C"), which inhibits the formation of nanotubes by poisoning the growth catalyst and can also cause short circuits on the substrate surface, the carbon source (typically, C_2H_2 or CH_4) is combined with a hydrogen-rich gas (typically, NH_3 or H_2), which produces reactive species in the plasma to remove any excess carbon. The use of etch gas during the growth process of CNTs is important. It has been widely reported that atomic hydrogen is the active species for the removal of excess carbon. NH_3 has a key role in removing any excess carbon through the generation of reactive atomic hydrogen species, which combine with and carry away carbon atoms. At high NH_3 ratios, NH_3 decomposes preferentially over C_2H_2. This is because the chemical bonds that hold the NH_3 molecule together are weaker than those that hold C_2H_2 together. This allows the C_2H_2 to decompose slowly, generating the small amounts of carbon necessary for nanotube self-assembly. At high C_2H_2 ratios, there is insufficient NH_3 to effectively suppress C_2H_2 decomposition, resulting in higher levels of carbon generation and deposition of excess carbon as a-C. NH_3 therefore has two key roles in the formation of carbon nanotubes: Not only does it generate atomic hydrogen species to remove any excess carbon, it also suppresses the decomposition of C_2H_2, limiting the amount of carbon generated in the first place. The gas–phase removal of carbon-containing species results in the production of gaseous HCN, which is detected in the mass spectra [24].

Production of CNTs was carried out by PECVD technique on different substrates; p-type boron doped silicon wafers (0.01–0.02 Ω cm range), high-purity quartz (SiO_2) microfiber filters (Whatmantm, UK) (QF), carbon paper and copper foil (Cu 000720/31, thickness 0.25 mm, purity 99.9 %). Prior to every vacuum process, the pressure in the corresponding reactor was lowered to the level below 4×10^{-4} Pa to ensure clean deposition conditions. In a first step, sputtering of Fe catalyst was performed to deposit 3 nm of metal using a 2 Pa and 50 W ArRF (radio frequency)-plasma. CNTs growth was carried out at 680 °C, during 900 s and using 50 W RF power in the presence of NH_3/C_2H_2 gas mixture. NH_3 is used as a carrier gas and C_2H_2 is the precursor gas (Table 1 for silicon wafer and carbon paper substrates). Figure 1a shows vertically aligned CNTs grown on silicon wafer; inset shows amorphous carbon on the tips of CNTs, which is a byproduct of the PECVD growth. In the case of QF, in a first attempt, the sample was heated using a PID Xantrex heater (XDC 60-100) controlled by a pyrometer. However, due to the fibrous nature of the quartz filter the radiation emitted by the heating element was scattered in all directions. As a consequence, the temperature measured by the pyrometer corresponded to that of the heating element and not of the substrate. In

Parameter	Value
Catalyst layer thickness	3 nm
Annealing time	870 s
PECVD process temperature	680 °C
PECVD process plasma power	50 W
PECVD process time	900 s

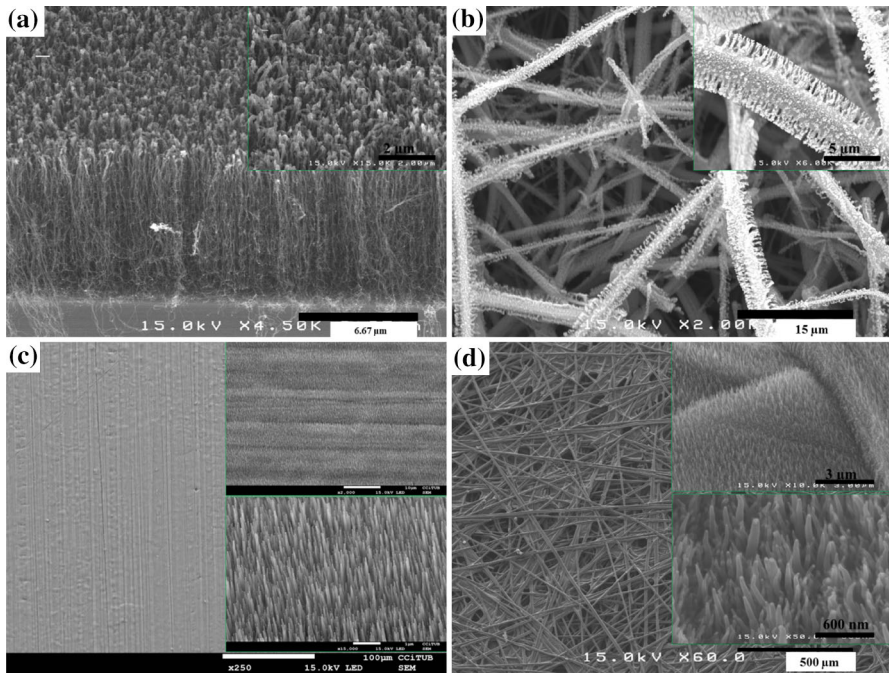**Table 1** Summary of the VACNTs growth conditions [82]

Fig. 1 MWCNTS grown by PECVD on **a** silicon wafer, **b** quartz filter [25], **c** copper foil [26] and **d** carbon paper

order to correct this, the power supplied to the heater while annealing a silicon wafer under the same conditions, was applied to our quartz filters. The growth temperature was set at 730 °C and growth time 30 min (see Fig. 1b) [25]. Figure 1c shows CNTs grown on copper foil. For this purpose, the native oxide layer on copper was removed by hydrogen plasma and then, a multi-layer configuration (Cu/Ni/Ti/Al$_2$O$_3$) was employed to increase the adhesion of an alumina buffer layer [26]. The rest of the parameters were the same as in Table 1, only the growth time was increased up to 30 min. As observed in Fig. 1c, under these conditions the CNTs grow all over the copper substrate homogeneously and without cracking. The nanotubes are vertically aligned, highly dense and long. Figure 1d shows vertically aligned CNTs grown on carbon paper and covering the whole surface.

The synthesis of SWCNTs requires the use of special plasma configuration such as remote plasma or point arc discharge, whereby the substrates were minimally exposed to the plasma sheath. In the plasma sheath, high density of plasma ion flux bombardment at sufficiently high energy caused C–C bond breakage. The presence of plasma radicals such as NH$_x$ and H further chemically etched the surface of the carbon nanotubes. The growth mechanism of SWCNT in a PECVD process determines the endurance of the carbon nanotubes towards ion-etching effects. In the tip-growth mechanism, the catalyst at the tip of the vertically growing SWCNT, offered protection to walls of the nanotube from the ion etching effects. On the other hand, in base-growth mechanism, the catalyst adhered to the substrate, and the

vertically growing SWCNTs had uncapped tips, which are easily destroyed by the impinging ions [27]. In a typical plasma, ions constitute only one part per million of the total number of the gas species, whereas the fraction of neutral radicals is of the order of 1 %. Therefore, the growth is essentially due to the neutral radicals (and species that form due to mutual collisions of these radicals as they move towards the substrate across the dark space) [28, 29].

Etchant gas (NH_3, H_2) makes an impact on the morphology (cylindrical or bamboo like) of the CNTs. Gohier et al. studied the effect of etchant gases (H_2 and NH_3) on the CNTs structure in a PECVD growth process. Ions produced in H_2 (H^+ or H^{3+}) are significantly lighter than those generated in NH_3 (NH^{3+}, NH^{2+}, NH^+, …). Therefore, ion physical etching is drastically reduced and ion effects on the CNT structure are reduced (but not suppressed). Second, concerning the chemical etching, H2 plasma produces less hydrogen radicals than NH_3 related to its higher dissociation energy (H–H: 4.52 eV vs H–NH_2: 1.92 V). Hence, there is reduction of carbon etching using H_2 plasmas compared to NH_3 plasma [30]. The role of nitrogen or nitrogen containing species based precursor gas and hydrogen on CNTs has been studied by Srivastava et al. They proposed morphology based growth model (bamboo like or hollow tubes) related to the nitrogen concentration in precursor etchant gas [31] (Fig. 2).

Introduction of nitrogen facilitates the precipitation of graphite sheets at the top surface of the catalyst particles and formation of curved structures. Compartment formation occurs because of periodic precipitation of graphite sheets on the top of catalyst particle. Outer diameter of growing tube is confined by size of the catalyst particle. Shape of the tip is controlled by the local geometry of the catalyst particle seeding the growth of the tube. The particles are in liquid or semi-liquid state during the growth. The elongation of catalyst particles into a truncated cone shape could be due to interaction between inner graphitic walls of growing compartment and the catalyst particle to acquire minimum energy configuration. In C_2H_2/NH_3 plasma, H and CN keep the surface of iron catalyst clean in the nucleation as well as post nucleation stages by gas phase and surface reactions. This leads nucleation and growth of high density aligned CNTs. NH_3 can easily be dissociated due to weaker bonds compared to that of H_2 or N_2. The observation of bamboo-structure in
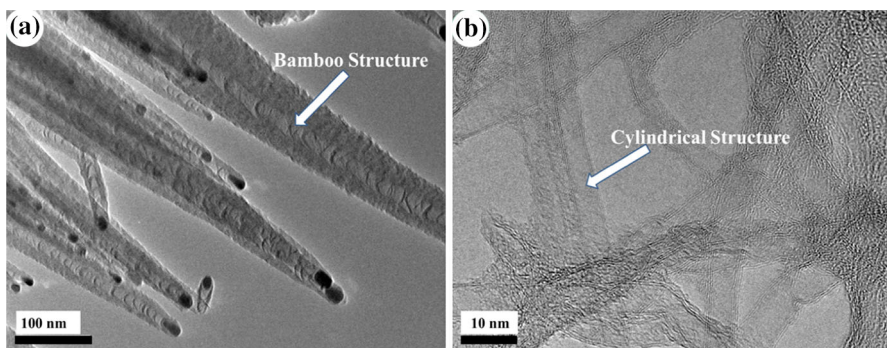

Fig. 2 **a** PECVD grown CNTs C_2H_2/NH_3 (1:2), **b** Water assisted grown CNTs C_2H_2/H_2 (1:2) water vapors

nitrogen containing plasma and hollow tubes in nitrogen-free plasma suggests that nitrogen or CN played critical role in compartment formation. Further it is believed that CNTs growth occurs via surface diffusion (SD) and/or bulk diffusion (BD) of carbon species through catalyst particles.

It was suggested that CNTs growth was governed by both SD and BD in presence of nitrogen and hence CN. Compartment formation was controlled mainly via BD process. On the other hand SD was responsible for growth of nanotube walls. High concentration of CN promoted BD of carbon through Fe particles and suppressed SD by keeping the catalyst surface clean and hence, shorter compartment length (CL). There is a possibility of CN diffusion through the Fe particles as well. But CN or N has very limited solubility in Fe so the concentration of N or CN in Fe is supposed to be very less compared to carbon [31].

Water Assisted CVD

Several studies have demonstrated the possibility to grow ultra-long forests of single-walled CNTs (SWCNTs) and multiwall CNTs (MWCNTs) (up to several millimeters in length) by means of water-assisted chemical vapor deposition (WACVD), oxygen-assisted microwave plasma chemical vapor deposition techniques and CO_2 assisted floating-ferrocene [32–35].

In general, the CNT yield for the SiO_2-supported Fe catalyst is much lower than for Fe supported on Al_2O_3. Upon annealing Fe makes oxides with the surface oxygen atoms of Al_2O_3 support. The Al_2O_3 support tends to stabilize interfacial Fe oxidation states, and prevents excessive coalescence of Fe particles. On the other hand, on SiO_2, Fe coalesces into larger islands. The reason behind this is Fe de-wets SiO_2 so that some areas become completely Fe-depleted. The resulting Fe nanoislands coarsen by cluster migration or Ostwald ripening. The coalescence is driven by a minimization of the surface free energies and the free energy of the support-metal interface [36]. Catalyst oxidation state plays an important key role in the growth process of CNTs because the catalyst is active in metallic state [37]. Teblum et al. showed that catalyst activity increased by the following order: $FeO < Fe_2O_3 < Fe_3O_4 <$ metallic Fe. Hata et al. performed water assisted growth of CNTs and found water acts in promoting and preserving catalytic activity, water acts as a weak oxidizer that would selectively remove amorphous carbon but would not damage the nanotubes at the growth temperature, because coating of the catalyst particles by amorphous carbon during chemical vapor deposition (CVD) reduces their activity and life time. Water-stimulated catalytic activity results in the growth of dense and vertically aligned SWCNT forests with millimeter-scale height in a 10-min growth time [32]. The role of water is to constrain the catalyst ripening by producing large amounts of OH groups on carbon, keep catalyst particles clean from amorphous carbon and active for continuous growth [38].

$$C(s) + H_2O(g) \rightarrow CO(g) + H_2(g)$$
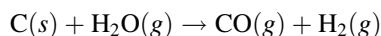
Recently, Hussain et al. reported structural evolution of CNTs during water assisted growth and found that, after a certain growth time, growth rate becomes slower, the

etching rate of the growing nanotubes outer planes increases extremely, and the nanotubes structure changes from curly to aligned. As a result of the etching, vertically aligned nanotubes with few walls (one to three) and large diameters are obtained [39]. This leads to a more ordered and highly dense mat of CNTs as observed in Fig. 3. Experimental conditions were as follows; first a 10 nm buffer layer of alumina was deposited by magnetron sputtering. Afterwards, 2 nm thick layer of Fe catalyst was sputtered on the alumina deposited substrate. Annealing of catalyst thin film was done at temperatures up to 600 °C with a ramp time of 750 s in a reducing atmosphere of hydrogen (100 sccm) at a pressure of 2 mbar. After a hold time of 120 s the pressure inside the reactor was lowered down to 1 mbar and C_2H_2 was introduced in the chamber (100 sccm). Then, the temperature was rapidly increased during the next 10 s up to 700 °C. The water flask outlet was opened
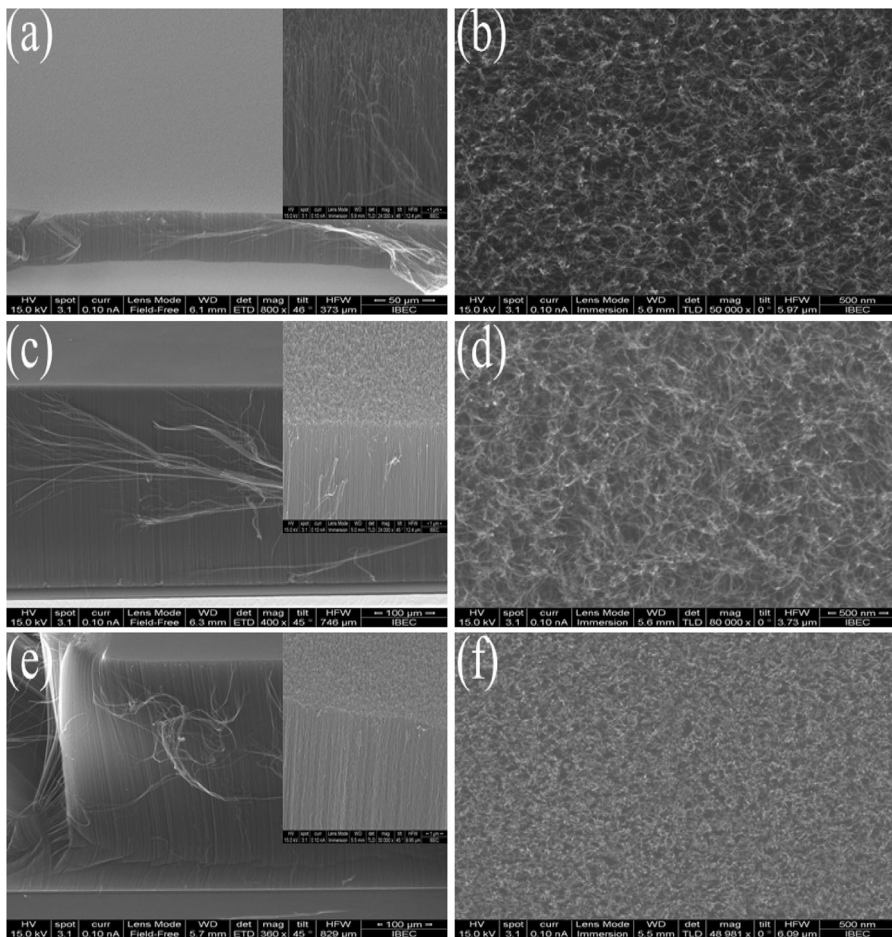

Fig. 3 SEM images of samples A (**a**, **b**), B (**c**, **d**) and C (**e**, **f**), with 5, 30 min and 1 h growth times, respectively. Side (**a**, **c**, **e**) and top (**b**, **d**, **f**) views [39]

$\sim$15 s after the introduction of C_2H_2. The calculated water flow was 0.04 sccm, controlled by opening $\sim$0.5 mm the circular scale of a metering valve.

Three samples of CNTs were grown with different growth times; sample A: 5 min, B: 30 min and C: 1 h (see Fig. 3). CNTs which are aligned by crowding effects alone tend to exhibit a greater degree of random orientation and entanglement in the tip region as compared to other areas of forest. The entangled "canopy" of a CNT forest can be removed with additional processing after growth, e.g., plasma etching, to create more alignment [40]. In this case no further treatment required to remove the "canopy" (see Fig. 3b, d, f). Increasing the growth time up to 3600 s (sample C), RBM (radial breathing modes) appear and the D, G and G' peaks become broader (see Fig. 4). The distinct appearance of RBM for sample C demonstrates that the outer layers of CNTs are being consumed during continuous growth, which leads to the formation of SWCNTs and double wall CNTs.

Plasma Functionalization

Oxygen Containing Plasma

Basically, CNTs have two areas with different reactive sites: the fullerene-like tube ends and the less reactive hexagonal cylindrical tube walls. Oxygen-based functionalization by plasma techniques can lead to morphological and chemical
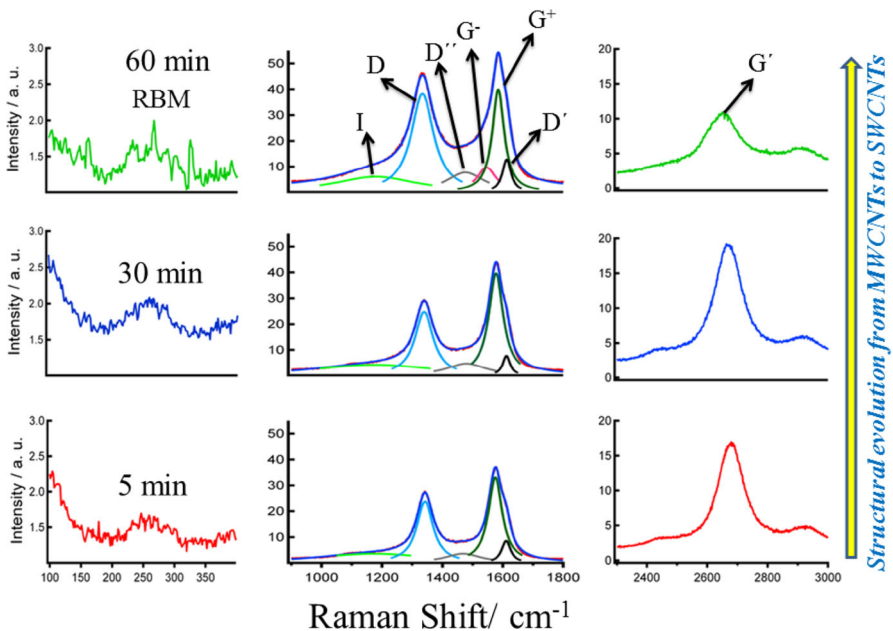

Fig. 4 Raman spectra of samples A, B and C in three different frequency regions. *Graphs* in the middle column show the peaks obtained from the fitting process [39]

modifications of the nanomaterials (Figs. 5, 6) [41]. The carbon bonds at the tips are under higher strain due to their large curvature and provide an area of enhanced reactivity and lower activation energy for oxidation reactions; therefore, oxidation is expected to start at the tips rather than at the cylindrical walls [42]. A plasma oxidation technique is usually used to remove amorphous carbon, Fe particles and to functionalize the surface of CNTs by introducing various oxygen functional groups such as carboxyl and hydroxyl groups [41, 43, 44]. These functional groups on the side walls of CNTs are favorable to contribute as a faradaic capacitance in total capacitance of the supercapacitor in aqueous solution. While for non-aqueous solutions they are not good because they are easily decomposed at 1.2 V and release some gases [45].

Oxygen plasma treatment is an effective way for modifying the carbon nanotube with proper parameters. However, the direct discharge can graft polar function more quickly but longer exposure time or higher energy can destroy the carbon nanotube [44]. Chen et al. adopted microwave-excited Ar/O_2 surface-wave plasma (SWP) treatment to functionalize the MWCNTs. They proposed an oxidation mechanism based on based on XPS analysis which shows how oxygen containing groups such as C–O, C=O and O–C=O were generated on the MWCNTs [46]. Saito et al. used oxygen pulsed—DC plasma treatment, which causes exfoliation of VACNTs tips,
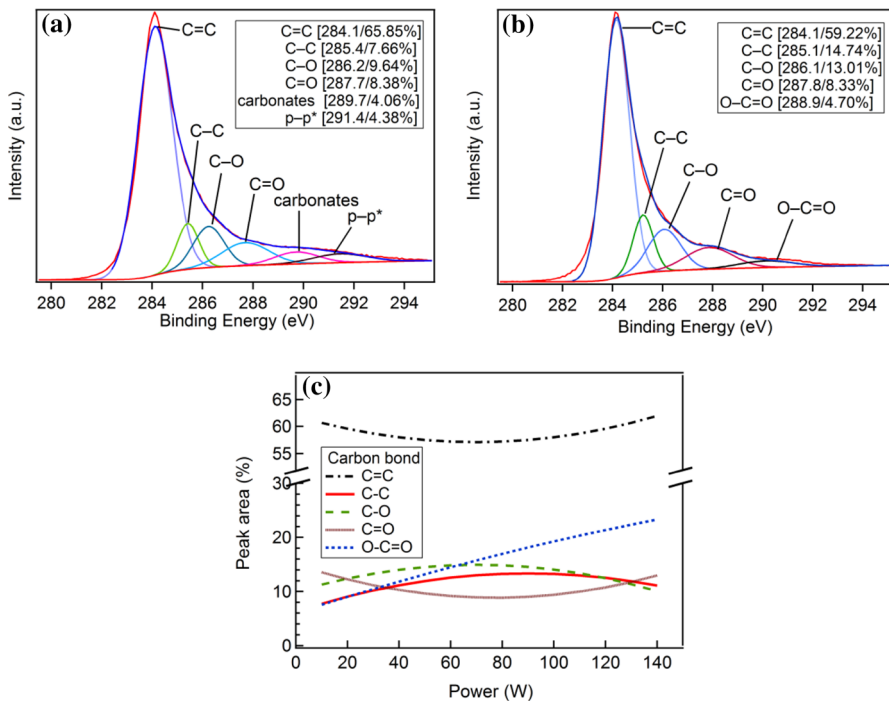

Fig. 5 XPS spectra of untreated MWCNTs (a) and MWCNTs treated with H_2O plasma at 140 W and 135 Pa (b). Percentage area of different carbon–carbon and carbon–oxygen bonds as a function of plasma power at a constant pressure of 50 Pa (c) [41]
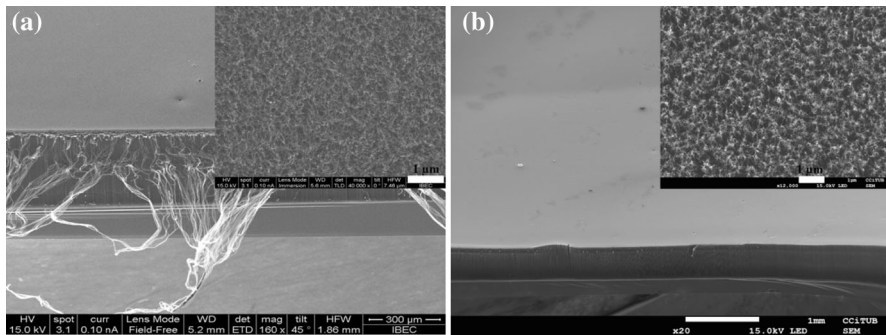
Fig. 6 SEM images of water assisted CVD grown CNTs; **a** untreated CNTs and **b** water plasma treated CNTs. *Inset* shows top view of the CNTs mat

and simultaneously functionalizes the CNTs with oxygen groups [47]. Vandsburger et al. studied the effect of electron bombardment during the plasma treatment on the degradation of MWCNTs and found that MWCNTs acts as nanostructured anode that accelerate and focus electron bombardment [48]. Ar/O_2 plasma is more efficient for oxygen functionalization than Ar plasma, possibly because of the more abundant active oxygen that exists in Ar/O_2 plasma, which may react with C radicals easily to generate more oxygen-containing functional groups [49]. Oxygen plasma has been successfully applied in sensors and devices to activate the surface of CNTs and improve their sensing properties [50, 51].

Ar/H_2O plasma treatment can significantly enhance the content of oxygen, and modify surface microstructure properties [52]. Peng et al. increased the oxygen functional groups on the surface of CNTs using a plasma treatment with a mixture of water/ozone, even at a low ozone concentration [53]. Lee et al. treated MWCNTs with an atmospheric pressure plasma source using an argon/water mixture and found OH plasma not only selectively reacts with impurities such as catalyst and amorphous carbon, but also attacks highly defective sites, carbon atoms with dangling bonds, and nanotube ends of MWCNTs [54].

A pure water plasma interacts chemically with the nanotubes and physically by an intense protonic bombardment, while an argon mixture includes physical effects (sputtering) and reduces the chemical effects. Hussain et al. used pure water vapor plasma treatment to remove amorphous carbon, catalyst particles and decrease the diameter of MWCNTs. They successfully crafted the desired oxygen functional groups by only changing two operational parameters (RF power and water pressure) [41]. They also proposed a two-step oxidation mechanism in which the carbon atoms are oxidized to C-O in a first step, and finally to O–C=O in a second step (Fig. 5c).

Untreated CNTs grown by water assisted CVD (i.e., CNTs without post-plasma treatment) present a typical morphology of vertically-aligned CNT forests with spaghetti-like surface, as shown in Fig. 6a. After plasma treatment, the CNT forests show significant change in their surface morphology. Randomly-distributed small bundles were observed with nanotube tips agglomerated together (Fig. 6b). During

plasma treatment, the surface energy of CNTs can be increased due to defects and functional radicals introduced physically or chemically by plasma; this can cause the CNTs' tips to coalesce and form CNT bundles to reduce the surface energy [55]. Zaho et al. made a detailed study to understand the plasma functionalization of ultralong CNTs forest by Ar/O_2 at different concentrations by using RF power supply. They found that, the interior nanotubes in the forest were not modified and oxygen-containing functional groups were not grafted successfully even be treated for long time by Ar + O_2 plasma and concluded that due to possible electromagnetic shielding of CNTs, plasma may not penetrate thick CNT forests to functionalize the nanotubes inside the forests [49].

Nitrogen Containing Plasma

The introduction of nitrogen containing functional groups onto the CNTs surface is known to promote faradaic pseudocapacitive reactions. Among these functional groups pyridinic and pyrrolic enhance the capacitive behavior, while quaternary nitrogen and pyridinic-*N*-oxide improve the electronic transfer [56, 57]. Kalita et al. modified the surface of MWCNTs with imine, amine, nitride and amide functional
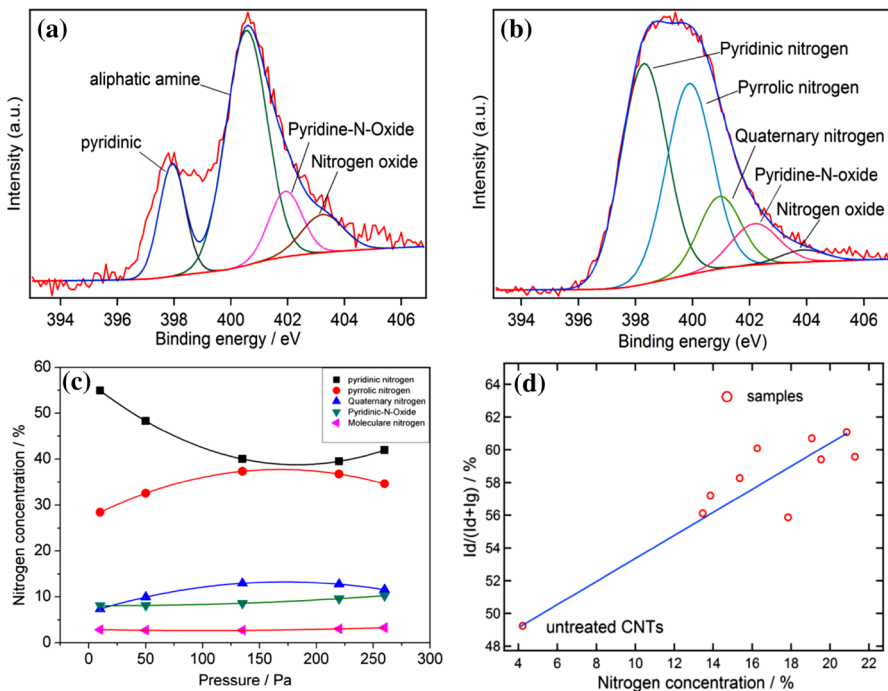

Fig. 7 **a**, **b** High resolution deconvoluted N 1s spectra of untreated and nitrogen-plasma treated MWCNTs, respectively. *Red* and *blue curves* correspond to experimental data and obtained fitting. **c** Nitrogen concentrations at a constant power of 75 W against nitrogen pressure, **d** structural disorder with respect to the nitrogen concentration. The *solid lines* are drawn to guide the eyes [58] (Color figure online)

groups by performing $N_2 + Ar$ plasma under surface wave microwave plasma irradiation [52]. On this subject, different methodologies have been applied to introduce nitrogen functionalities on the CNTs surface. Hussain et al. significantly introduced nitrogen containing groups in MWCNTs and removed amorphous carbon by using radio frequency nitrogen plasma (Fig. 7a, b) [26, 58]. Nitrogen functionalities were successfully incorporated such as quaternary nitrogen at the basal planes and pyrrolic nitrogen at the edge surface on the MWCNTs by controlling two operation parameters; RF power and nitrogen pressure.

In order to study the different types of nitrogen incorporated in MWCNTs high resolution N 1s spectra were deconvoluted into four and five peaks for untreated and nitrogen plasma treated MWCNTs, respectively (Fig. 7c, d. The peaks of untreated MWCNTs found at (398.1 ± 0.2), (400.5 ± 0.2), (401.8 ± 0.2) and (403.6 ± 0.2) eV are assigned to pyridinic nitrogen functionalities, aliphatic amine [59], pyridine-N-oxide and nitrogen oxide [60, 61], respectively. The presence of nitrogen-based functionalities in the untreated sample is due to the use of NH_3 during the growth process. For nitrogen plasma treated MWCNTs the peaks observed at (398.1 ± 0.2), (399.6 ± 0.2), (400.8 ± 0.2), (401.9 ± 0.2), and (403.6 ± 0.2) eV were assigned to pyridnic nitrogen [62], pyrrolic nitrogen [62], quaternary nitrogen [63] pyridinic-N-oxide, and nitrogen oxide, respectively. It should be noted that the quaternary nitrogen peak arises due to the presence of nitrogen substitutes in the aromatic graphene sheet. Except for this functionality, all nitrogen containing groups introduced on the CNTs are located at the edges of graphene layers. From the obtained results (see Table 2 it is clear that the nitrogen plasma treatment produces new functionalities like quaternary and pyrrolic-like nitrogen and increases the concentration of pyridine functionalities [60]. Figure 7c shows the concentration of different nitrogen groups as a function of nitrogen pressure at a constant power of 75 W obtained from a polynomial model. At low pressure the relative amount of pyridinic nitrogen is high, and presents a minimum at a pressure of 220 Pa, while the relative percentages of pyrrolic and quaternary

Table 2 Relative percentages of the bonds obtained after fitting the XPS N1s spectra [58]

MWCNTs (NP)	Pyridinic nitrogen (%)	Pyrrolic nitrogen (%)	Quaternary nitrogen (%)	Pyridine-N-oxide (%)	Nitrogen oxide (%)
Untreated	20.54	54.64[a]	–	15.51	9.31
10 W, 135 Pa	41.26	35.76	12.41	7.94	2.63
29 W, 50 Pa	39.93	38.54	11.96	6.78	2.78
29 W, 220 Pa	38.74	37.34	12.67	7.15	4.14
75 W, 10 Pa	44.57	36.68	9.97	5.84	2.92
75 W, 135 Pa	38.9	36.51	14.24	7.51	2.84
75 W, 260 Pa	40.56	36.17	7.27	7.27	2.32
121 W, 50 Pa	46.23	34.86	10.81	5.19	2.92
121 W, 220 Pa	41.36	38.17	10.3	7.37	2.78
140 W, 135 Pa	46.67	36.54	6.67	6.97	3.06

[a] For this sample the percentage corresponds to aliphatic amine

nitrogen show a maximum at middle pressures. On the contrary, no big change is observed in the relative percentages of pyridinic-*N*-oxide and molecular nitrogen. Only a slight increase can be appreciated for oxygenated nitrogen at higher pressures. In view of these results we assume that at low pressures a small amount of nitrogen replaces carbon atoms in the six fold ring forming pyridinic nitrogen, which stops the propagation of further nitrogen functionalities [50, 64]. With increasing nitrogen pressure the plasma becomes more effective resulting in an increase of the pyrrolic and quaternary nitrogen amounts at the edge and basal planes, respectively. At higher pressures the percentage of pyridinic nitrogen and pyridinic-*N*-oxide increases again resulting in a decrease of the pyrrolic and quaternary nitrogen, which is in agreement with other reports on annealed coals and carbonized nitrogen-containing model compounds [65].

Metal Oxide/CNTs

Functionalization of CNTs using metal oxides allows the synthesis of new functional materials with improved electrochemical and catalytic properties. Several metal oxides have been investigated such as TiO_2, SnO_2, ZnO, NiO or MnO_2. The obtained metal oxide/CNTs nanocomposites show enhanced performance in different sensors and devices. For example, TiO_2/CNTs have been used to improve the photocatalytic activity of the oxide [66, 67] and the anode performance in microbial fuel cells [68]. SnO_2/CNTs composite presents highly reversible lithium storage [69] and ZnO/CNTs improve the performance of anodes in lithium ion batteries [70] and optoelectronic devices [71]. NiO/CNTs composites have found application as electrode material in supercapacitors [72] as well as in biosensors [73].

Carbon nanotubes coated with a thin layer of manganese dioxide have been proven to increase the performance of supercapacitors. In electric double layer capacitors (EDLC) the capacitance is mainly attributed to the physical adsorption of ions at the electrode/electrolyte interface as a non-faradic behavior, with a contribution of 1–5 % pseudocapacitance in the case of carbon. While in faradic capacitors (pseudocapacitors) the charge storage mechanism is mainly provided by the contribution of reversible redox reactions that take place on the electrode surface involving various oxidation states of metal oxides and the physical adsorption of ions [74]. Capacitance enhancement of carbon electrodes can be achieved by surface specific treatments that introduce various kinds of functional groups such as oxygen and nitrogen based functionalities. As a result, the electrodes exhibit an increase of the double layer capacitance, and also, of reversible faradic reactions that contribute to the charge storage as a pseudocapacitance [41, 58]. Generally, pseudocapacitance is associated with reversible faradic redox processes in various oxidation states of transition metal oxides (RuO_2, MnO_2, NiO, V_2O_5, IrO_2). For supercapacitor applications it is important that the electrode material possess high surface area, high porosity as well as very low electrical resistance. A suitable configuration is CNTs/MnO_2 composite electrodes, in which a thin layer of MnO_2 provides high pseudocapacitance due to faradic redox reactions taking place on

large surface area electrodes. CNTs provide high electrical conductivity and mechanical stability to the 3D-electrode (Fig. 8) [43]. Hou et al. suggested that the oxygen functional groups on the surface of CNTs act as nucleation sites for the growth of MnO_2. The Mn^{2+} ions in the solution are preferentially adsorbed on these sites due to electrostatic force between Mn^{2+} ions and polar oxygen functional groups on the surface of CNTs [75]. Hussain el al. found MnO_2/CNTs nanocomposites prepared by galvanostatic deposition method exhibit an increase in their specific capacitance from 678 Fg^{-1}, for untreated CNTs, up to 750 Fg^{-1}, for water plasma-treated CNTs [43].

Electrochemical Characterization

The electrochemical characterization of the samples is performed by cyclic voltammetry (CV). Figure 9a, b show a comparison between cyclic voltammograms of different CNTs samples at a scan rate of 50 mVs^{-1} (untreated MWCNTs, water plasma treated MWCNTs and nitrogen plasma treated MWCNTs) using a typical 3 electrode cell configuration and 0.1 M Na_2SO_4 as en electrolyte. For untreated CNTs the voltammogram presents a typical rectangular shape associated with the double layer capacitance behavior. Whereas the voltammograms of water plasma and nitrogen plasma treated samples show a slight deviation from this shape. This is related to pseudocapacitive (faradaic) processes due the presence of oxygen and nitrogen functional groups for water plasma and nitrogen plasma treated CNTs, respectively [41, 58]. Water plasma provides an especially high formation of C=O (quinone) groups on the CNTs surface. This type of groups promotes the adsorption of protons, which is in agreement with the non-perfect rectangular shape of the CV curves (i.e., a non-truly horizontal value of the current) [76].

The specific capacitance increases for all the water plasma treated MWCNTs from 23 up to 68 Fg^{-1} at a scan rate of 10 mVs^{-1} (see Table 3). The specific capacitance increases from 22 Fg^{-1} for untreated MWCNTs up to 55 Fg^{-1} for plasma treated MWCNTs. Although containing a relatively higher nitrogen concentration than untreated CNTs, the sample treated at 10 W plasma power
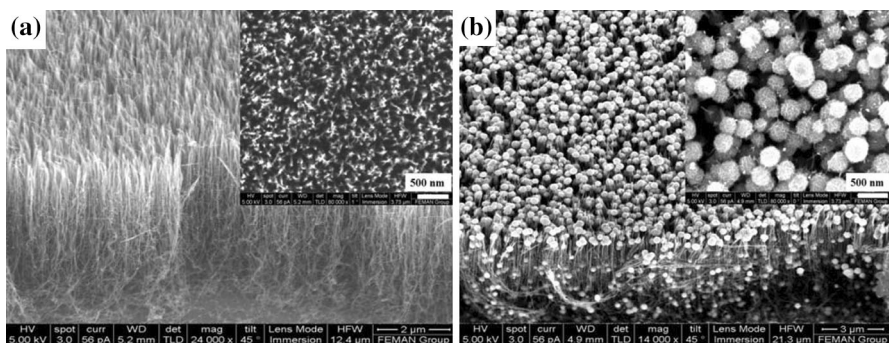

Fig. 8 **a** VACNTS without MnO_2 nanoflower and, **b** nanocomposite of VACNTs/MnO_2
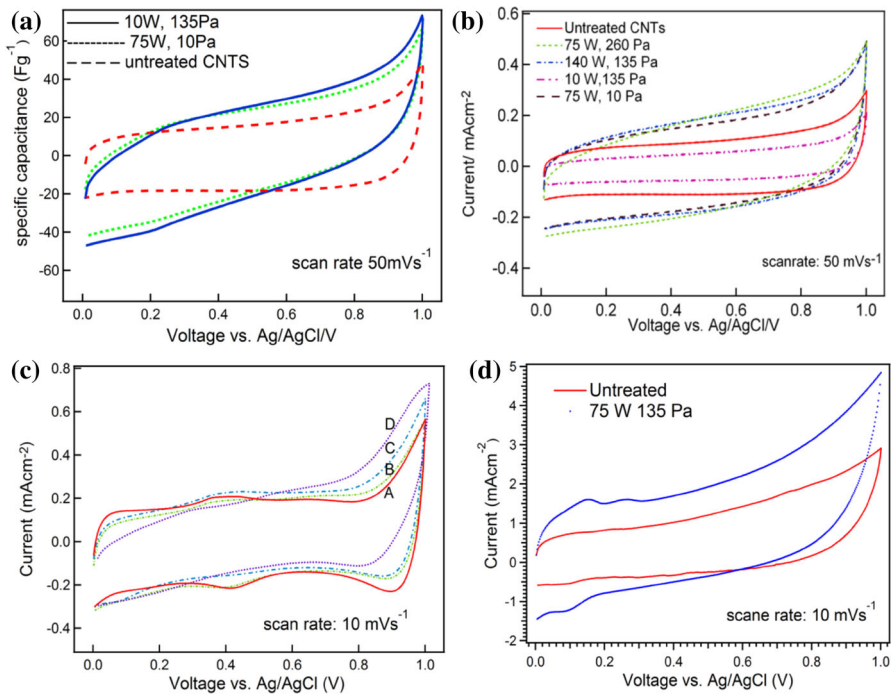
Fig. 9 Comparison of cyclic voltammograms of untreated and plasma treated CNTs **a** water plasma treated MWCNTs [41], **b** nitrogen plasma treated MWCNTs [58], **c** MWCNTs/MnO$_2$ and wpCNTs/MnO$_2$ under different plasma conditions [(A): untreated, (B): 75 W, 135 Pa, (C): 140 W, 135 Pa, (D): 10 W, 135 Pa] [43], **d** water assisted grown CNTs, transferred on aluminum tape and water plasma treated [39]

Table 3 Specific capacitances of untreated and nitrogen plasma (NP) [58], water plasma (WP) treated [41] and MnO$_2$ deposited water plasma treated MWCNTs [43] and water assisted CNTs transferred on aluminum tape [39] at a scan rate of 10 mVs^{-1}

| Sample | NP | WP | CNTs/MnO$_2$ | WA | Sample | NP | WP | CNTs/MnO$_2$ | WA |
	C_s (Fg^{-1})					C_s (Fg^{-1})			
MWCNTs	22	23	678	87	75 W, 135 Pa	34	27	669	148
10 W, 135 Pa	16	68	750	–	75 W, 260 Pa	55	41	696	–
29 W, 50 Pa	46	29	686	–	121 W, 50 Pa	41	24	669	–
29 W, 220 Pa	37	45	746	–	121 W, 220 Pa	46	37	665	–
75 W, 10 Pa	52	58	713	–	140 W, 135 Pa	50	22	694	–

and 135 Pa nitrogen pressure presents a specific capacitance below that of untreated nanotubes (16 Fg^{-1}) (see Table 3). Under these conditions the plasma treatment seems to effectively introduce nitrogen groups in the amorphous carbon but not to remove it, therefore blocking the pores and in turn the flow of electrolyte through the nanotubes. The rest of the treated samples present higher capacitance values

than untreated CNTs. Hence, the functional groups (oxygen and nitrogen) introduced by the treatment increase the charge storage capabilities of the nanotubes, whose wettability is further improved through the removal of amorphous carbon by the plasma [58].

The specific capacitance of untreated CNTs/MnO$_2$ composite is 678 Fg^{-1} and increases for most of the wpCNTs/MnO$_2$ composites. Highest specific capacitance (750 Fg^{-1}) was obtained using plasma-treated CNTs with 10 W RF power and 135 Pa water pressure as the nanocomposite electrode [43]. The increase in capacitance is related to the removal of amorphous carbon, soft etching, that is, less structural defects in comparison with other water plasma-treated carbon nanotubes, and the addition of oxygen functional groups. Under these water-plasma conditions (10 W, 135 Pa), the existence of quinone groups on the CNTs surface is especially high [18]. This type of groups improve the adsorption of protons, due to which shape of CV is deviated (see Fig. 9c). As a result, the specific capacitance significantly increases due to the additional contribution of faradic currents (I_F). Samples treated under other plasma conditions clearly show a redox peak in the potential region from 0.4 to 0.6 V that corresponds to reversible redox reactions between Mn^{4+} and Mn^{3+}. In the case of water assisted grown ultralong CNTs and transferred on Aluminum tape the specific capacitance increase from 87 to 148 Fg^{-1} for untreated to water plasma treated CNTs [39].

Gas–Phase Interactions Between VOCs and CNTs

A large number of households and industrials products contain volatile organic compounds (VOCs). VOCs can easily evaporate at room temperature and are extremely harmful for the health of human being. Among various types of VOCs, chlorinated compounds are used frequently in a wide range of industrial products and chemical processes, polluting the environment and ground water resources. Therefore, it is desirable to control the chlorinated VOCs emission in air by utilizing various kinds of adsorption / removal processes.

Usually, carbon based adsorbents are used for the removal of contaminants due to their high surface area. CNTs can adsorb a variety of gases and have been proven to be superior to activated carbon for the removal of dioxin 1,2-dichlorobenzene from water in a wide range of pH 3–10 [77]. The characteristics of CNTs suggest that they have strong interaction with organic molecules through non-covalent forces, hydrogen bonds, π–π interactions, for instance in polycyclic aromatic hydrocarbons (PAHs) [78], electrostatic forces and van der Waals forces. Three main interactions are responsible for the adsorptions of organic compounds by CNTs; hydrophobic effect, π-electron donor–acceptor (π-EDA) bonds and hydrogen bonds [79–81]. Amade et al. studied the VOCs characteristic desorption times by Quadruple mass spectroscopy-residual gas analyzer (SRS QMS-RGA-300, USA) increased from bare quartz filter (QF) to carbon nanotubes quartz filter (CNTsQF) and water plasma treated carbon nanotubes quartz filter (wp-CNTsQF). The latter being the one with the longest characteristic desorption times [71]. A water plasma treatment of the grown nanotubes introduced oxygen functional groups on their surface without
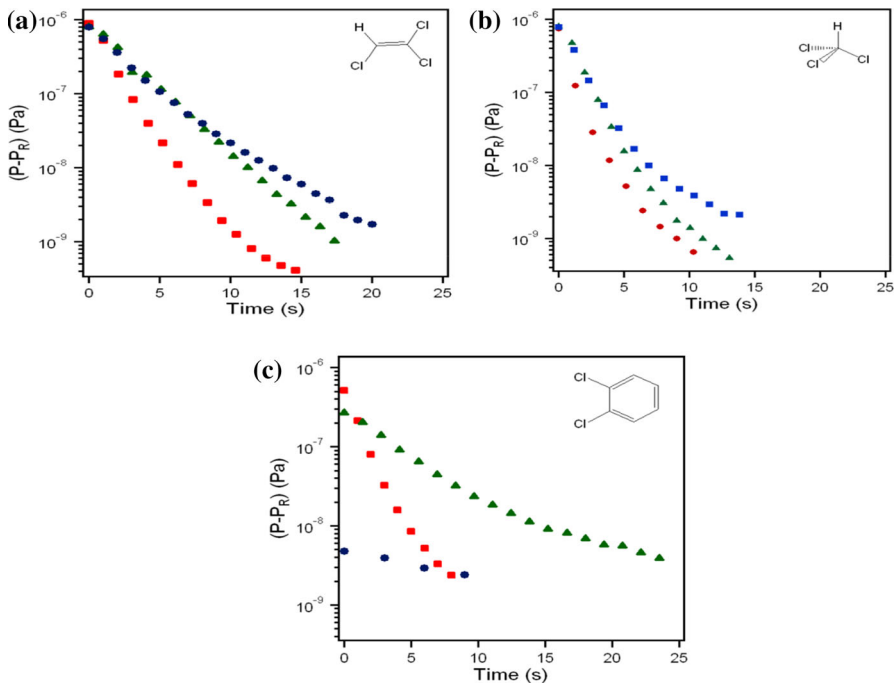
Fig. 10 Comparative desorption study. Desorption process of **a** trichloroethylene, **b** chloroform and **c** 1,2-dichlorobenzene. *Squares*: QF, *triangles*: CNTsQF and circles: WPCNTsQF [25]

modification of their alignment. The presence of inner cavities and functional groups on the CNTs surface contributes to improve their capability to remove or selectively detect organic pollutants. It has been proven that the adsorption/desorption capacity of chlorinated VOCs by CNTsQF and wp-CNTsQF is higher than that of bare QFs. In addition, the CNTsQF and wp-CNTsQF affinity for the adsorption/desorption of chlorinated VOCs increases with compound solubility in water and polarity. Finally, molecules with aromatic rings present stronger interactions with CNTs (π-stacking) and thus, significantly longer desorption times and time constants (Fig. 10) [25].

Conclusions

CNTs were successfully grown on different types of substrates (Si wafer, copper, MEAs (microelectrode arrays), carbon paper, and graphite) by means of hot wire radio frequency plasma chemical vapor deposition. SEM and HRTEM observations show vertically aligned nanotubes with a bamboo like- and multiwall structure. Water plasma treatment significantly removes amorphous carbon and functionalizes the surface of CNTs with different oxygen groups. Nitrogen plasma treatment

decorates the CNTs surface with various nitrogen based functional groups (pyridinic, pyrrolic and quaternary).

Water plasma is more effective over nitrogen plasma to remove amorphous carbon. Also, peeling of the outer planes of MWCNTs by water plasma is much faster than nitrogen plasma. Both nitrogen and water plasma raise the capacitance of CNTs notably in comparison to untreated CNTs. Manganese dioxide deposited by galvanostatic method on untreated CNTs and water plasma treated CNTs show an increase in the specific capacitance of the nanocomposite electrode.

Ultra long CNTs were synthesized by water assisted CVD using an alumina buffer layer between Fe (catalyst) and Si substrate. Water vapor enhances the crystallinity of growing nanotubes and their length increases with growing time. However, the presence of water vapor gradually changes their structure from multiwall to thinner one or, even, single wall carbon nanotubes. Adhesion of CNTs through the alumina buffer layer to the substrate is a key issue for the growth process of CNTs on copper. A multilayered configuration ($Cu/Ni/Ti/Al_2O_3$) prior to the catalyst deposition enhances the growth rate and quality of CNTs.

Vertically-aligned CNTs were synthesized on quartz fiber filters for environmental applications. The ability to detect or remove organic pollutants increases after the water plasma functionalization and also by removing the catalyst from the top of CNTs to provide the inner cavities for use. It was found that molecules with aromatic rings present stronger interactions with CNTs (π-stacking).

References

1. S. Ijima (1991). *Lett. Nat.* **354**, 56–58.
2. S. Iijima and T. Ichihashi (1993). *Nature* **363**, 603–605.
3. D. S. Bethune, C. H. Kiang, M. S. de Vries, G. Gorman, R. Savoy, J. Vasquez, and R. Beyers (1993). *Nature* **363**, 605–607.
4. M. M. J. Treacy, T. W. Ebbesen, and J. M. Gibson (1996). *Nature* **381**, 678–680.
5. A. Krishnan, E. Dujardin, T. W. Ebbesen, P. N. Yianilos, and M. M. J. Treacy (1998). *Phys. Rev. B* **58**, (15), 14013–14019.
6. B. Peng, M. Locascio, P. Zapol, S. Li, S. L. Mielke, G. C. Schatz, and H. D. Espinosa (2008). *Nat. Nanotechnol.* **3**, 626–631.
7. P. Kim, L. Shi, A. Majumdar, and P. L. McEuen (2001). *Phys. Rev. Lett.* **87**, 215502.
8. T. Belin and F. Epron (2005). *Mater. Sci. Eng. B* **119**, 105–118.
9. E. T. Thostenson, E. T. Z Ren, and T.-W. Chou (2001). *Compos. Sci. Technol.* **61**, 1899–1912.
10. H. J. Li, W. G. Lu, J. J. Li, X. D. Bai, and C. Z. Gu (2005). *Phys. Rev. Lett.* **95**, 086601.
11. S. Frank, P. Poncharal, Z. L. Wang, and W. A. de Heer (1998). *Science* **280**, 1744–1746.
12. S. J. Tans, M. H. Devoret, H. Dai, A. Thess, R. E. Smalley, L. J. Geerlings, and C. dekker (1997). *Nature* **386**, 474–477.
13. C. V. Haesendonck, L. Stockman, R. J. M. Vullers, Y. Bruynseraede, L. Langer, V. Bayot, E. Grivei, J.-P. Issi, J. P. Heremans, and C. H. Olk (1997). *Surf. Sci.* **386**, 279–289.
14. J. C. Charlier (2002). *Acc. Chem. Res.* **35**, 1063–1069.
15. E. V. Hooijdonk, C. Bittencourt, R. Snyders, and J. F. Colomer (2013). *Beilstein J. Nanotechnol.* **4**, 129–152.
16. C. N. R. Rao and A. Govindaraj, *Nanotubes and Nanowires*, 2nd Edition, RSC Nanoscience & Nanotechnology (2011). doi:10.1039/9781849732840-00001.
17. M. Kumar and Y. Ando (2010). *J. Nanosci. Nanotechnol.* **10**, 3739–3758.

18. R. T. K. Baker and D. J. C. Yates, *Filamentous Carbon Formation Over Iron Surfaces* (1983). doi:10.1021/bk-1983-0202.ch001. ISBN13: 9780841207455, eISBN: 9780841209848.

19. A. Gorbunov, O. Jost, W. Pompe, and A. Graff (2002). *Carbon* **40**, 113–118.

20. E. F. Kukovitsky, S. G. Lvov, and N. A. Sainov (2000). *Chem. Phys. Lett.* **317**, 65–70.

21. Y. Chen and J. Zhang (2011). *Carbon* **49**, 3316–3324.

22. S. Hofmann, C. Ducati, and J. Robertson (2003). *Appl. Phys. Lett.* **83**, (1), 135–137.

23. F. Javier del Campo, J. García-Céspedes, F. Xavier Muñoz, and E. Bertran (2008). *Electrochem. Commun.* **10**, 1242–1245.

24. M. S. Bell, K. B. K. Teo, R. G. Lacerda, W. I. Milne, D. B. Hash, and M. Meyyappan (2006). *Pure Appl. Chem.* **78**, (6), 1117–1125.

25. R. Amade, S. Hussain, I. R. Ocaña, and E. Bertran (2014). *J. Environ. Eng. Ecol. Sci.* **3**, 1–7.

26. S. Hussain, R. Amade, H. Moreno, and E. Bertran (2014). *Diam. Relat. Mater.* **49**, 55–61.

27. H. Lim, Z. Luo, Z. Shen, and J. Lin (2010). *Nanoscale Res. Lett.* **5**, 1377–1386.

28. V. I. Merkulov, A. V. Melechko, M. A. Guillorn, D. H. Lowndes, and M. L. Simpson (2002). *Chem. Phys. Lett.* **361**, 492–498.

29. Z. Luo, S. Lim, Y. You, J. Miao, H. Gong, J. Zhang, S. Wang, J. Lin, and Z. Shen (2008). *Nanotechnology* **19**, 255607.

30. A. Gohier, T. M. Minea, M. A. Djouadi, and A. Granier (2007). *J. Appl. Phys.* **101**, 054317.

31. S. K. Srivastava, V. D. Vankar, and V. Kumar (2006). *Thin Solid Films* **515**, 1552–1560.

32. K. Hata, D. N. Futaba, K. Mizuno, T. Namai, M. Yumura, and S. Iijima (2004). *Science* **306**, 1362–1364.

33. G. Zhang, D. Mann, L. Zhang, A. Javey, Y. Li, E. Yenilmez, Q. Wang, J. P. McVittie, J. Gibbons, and H. Dai (2005). *PNAS* **102**, (45), 16141–16145.

34. Y. Kim, W. Song, S. Y. Lee, S. Shrestha, C. Jeon, W. C. Choi, M. Kim, and C. Y. Park (2010). *Jpn. J. Appl. Phys.* **49**, 085101.

35. X. Yang, L. Yuan, V. K. Peterson, Y. Yin, A. I. Minett, and A. T. Harris (2011). *J. Phys. Chem. C* **115**, 14093–14097.

36. C. Mattevi, C. T. Wirth, S. Hofmann, R. Blume, M. Cantoro, C. Ducati, C. Cepek, A. Knop-Gericke, S. Milne, C. Castellarin-Cudia, S. Dolafi, A. Goldoni, R. Schloegl, and J. Robertson (2008). *J. Phys. Chem. C* **112**, 12207–12213.

37. E. Teblum, Y. Gofer, C. L. Pint, and G. D. Nessim (2012). *J. Phys. Chem. C* **116**, 24522–24528.

38. K. Xie, M. Muhler, and W. Xia (2013). *Ind. Eng. Chem. Res.* **52**, (39), 14081–14088. doi:10.1021/ie401829e.

39. S. Hussain, R. Amade, and E. Bertran (2014). *Mater. Chem. Phys.* **148**, 914–922.

40. J. J. Nguyen, T. L. Bougher, P. P. S. S. Abadi, and A. Sharma (2013). *J. Micro Nano-Manuf.* **1**, 014501–014505.

41. S. Hussain, R. Amade, E. Jover, and E. Bertran (2012). *Nanotechnology* **23**, 385604.

42. J. E. Fischer, in Y. Gogotsi (ed.), *Carbon Nanotubes: Structure and Properties Nanotubes and Nanofibers* (Taylor Francis, Boca Raton, FL, 2006), p. 36.

43. S. Hussain, R. Amade, E. Jover, and E. Bertran (2013). *Sci. World J.* Article ID 832581, 8.

44. T. Xu, J. Yang, J. Liu, and Q. Fu (2007). *Appl. Surf. Sci.* **253**, 8945–8951.

45. Y. Yu, C. Cui, W. Qian, Q. Xie, C. Zheng, C. Kong, and F. Wei (2013). *Asia-Pac. J. Chem. Eng.* **8**, 234–245.

46. C. Chen, B. Liang, A. Ogino, X. Wang, and M. Nagatsu (2009). *J. Phys. Chem. C* **113**, 7659–7665.

47. E. Saito, E. F. Antunes, H. Zanin, F. R. Marciano, A. O. Lobo, V. J. Trava-Airoldi, and E. J. Corata (2014). *J. Electrochem. Soc.* **161**, (5), H321–H325.

48. L. Vandsburger, S. Coulombe, and J. L. Meunier (2013). *J. Phys. D Appl. Phys.* **46**, 485301.

49. B. Zhao, L. Zhang, X. Wang, and J. Yang (2012). *Carbon* **50**, 2710–2716.

50. Z. Zanolli, R. Leghrib, A. Felten, J.-J. Pireaux, E. Llobet, and J.-C. Charlier (2011). *ACS Nano.* **5**, 4592–4599.

51. H. Muguruma, Y. Shibayama, and Y. Matsui (2008). *Biosens. Bioelectron.* **23**, 827–832.

52. C. Chen, A. Ogino, X. Wang, and M. Nagatsu (2010). *Appl. Phys. Lett.* **96**, 131504.

53. K. Peng, L. Q. Liu, H. Li, H. Meyer, and Z. Zhang (2011). *Carbon* **49**, 70–76.

54. S. Lee, J.-W. Peng, and C. H. Liu (2008). *Carbon* **46**, 2124–2132.

55. Z. Hou, B. Cai, H. Liu, and D. Xu (2008). *Carbon* **46**, 405–413.

56. D. Hulicova-Jurcakova, M. Seredych, G. Q. Lu, and T. J. Bandosz (2009). *Adv. Funct. Mater.* **19**, 438–447.

57. L. Li, E. Liu, H. Shen, Y. Yang, Z. Huang, X. Xiang, and Y. Tian (2011). *J. Solid State Chem.* **15**, 175–182.
58. S. Hussain, R. Amade, E. Jover, and E. Bertran (2013). *J. Mater. Sci.* **48**, 7620–7628.
59. W. Shen, Z. Li, and Y. Liu (2008). *Recent Pat. Chem. Eng.* **1**, 27–40.
60. C. Jones and E. Sammann (1990). *Carbon* **28**, (4), 509–514.
61. H. Wang, R. Cote, G. Faubert, D. Guay, and J. P. Dodelet (1999). *J. Phys. Chem. B* **103**, 2042–2049.
62. A. Toth, K. V. Voitko, O. Bakalinska, G. P. Prykhodko, I. Bertoti, A. Martínez-Alonso, J. M. D. Tascon, V. M. Gunko, and K. Laszlo (2012). *Carbon* **50**, 577–585.
63. J. R. Pels, F. Kapteijn, J. A. Moulijn, Q. Zhu, and K. M. Thomas (1995). *Carbon* **33**, 1641–1653.
64. S. Bhattacharyya, J. Hong, and G. Turban (1998). *J. Appl. Phys.* **83**, 3917–3919.
65. S. Biniak, G. Szymanski, J. Siedlewski, and A. Swiatkowski (1997). *Carbon* **35**, 1799–1810.
66. J. Yu, T. Ma, and S. Liu (2011). *Phys. Chem. Chem. Phys.* **13**, 3491–3501.
67. Y. Yu, J. C. Yu, J.-G. Yu, Y.-C. Kwok, Y.-K. Che, J.-C. Zhao, L. Ding, W.-K. Ge, and P.-K. Wong (2005). *Appl. Catal. A Gen.* **289**, 186–196.
68. Z. Wen, S. Ci, S. Mao, S. Cui, G. Lu, K. Yu, S. Luo, Z. He, and J. Chen (2013). *J. Power Sources* **234**, 100–106.
69. P. Wu, N. Du, H. Zhang, J. Yu, and D. Yang (2010). *J. Phys. Chem. C* **114**, 22535–22538.
70. S. M. Abbas, S. T. Hussain, S. Ali, N. Ahmad, N. Ali, and S. Abbas (2013). *J. Mater. Sci.* **48**, 5429–5436.
71. J. S. Park, J. M. Lee, S. K. Hwang, S. H. Lee, H.-J. Lee, B. R. Lee, H. I. Park, J.-S. Kim, S. Yoo, M. H. Song, and S. O. Kim (2012). *J. Mater. Chem.* **22**, 12695–12700.
72. A. D. Su, X. Zhang, A. Rinaldi, S. T. Nguyen, H. Liu, Z. Lei, L. Lu, and H. M. Duong (2013). *Chem. Phys. Lett.* **561–562**, 68–73.
73. H. Karimi-Maleh, P. Biparva, and M. Hatami (2013). *Biosens. Bioelectron.* **48**, 270–275.
74. B. E. Conway *Electrochemical Supercapacitors: Scientific Fundamentals and Technological Applications* (Kluwer Academic/Plenum Publishers, NewYork, NY, 1999).
75. Y. Hou, Y. Cheng, T. Hobson, and J. Liu (2010). *NanoLetters* **10**, 2727–2733.
76. C.-T. Hsieh and H. Teng (2002). *Carbon* **40**, (5), 667–674.
77. X. Peng, Y. Li, Z. Luan, Z. Di, H. Wang, B. Tian, and Z. Jia (2003). *Chem. Phys. Lett.* **376**, 154–158.
78. M. Kah, X. Zhang, M. T. Jonker, and T. Hofmann (2011). *Environ. Sci. Technol.* **45**, 6011–6017.
79. K. Yang, W. Wu, Q. Jing, and L. Zhu (2008). *Environ. Sci. Technol.* **42**, 7931–7936.
80. D. Lin and B. Xingt (2008). *Environ. Sci. Technol.* **42**, 7254–7259.
81. K. Yang, W. Wu, Q. Jing, W. Jiang, and B. Xing (2010). *Environ. Sci. Technol.* **44**, 3021–3027.
82. R. Amade, E. Jover, B. Caglar, T. Mutlu, and E. Bertran (2011). *J. Power Sources* **196**, 5779–5783.